

Article

Full-Scale Modeling and FBGs Experimental Measurements for Thermal Analysis of Converter Transformer

Fan Yang ^{1,*}, Sance Gao ¹, Gepeng Wang ², Hanxue Hao ¹ and Pengbo Wang ¹

¹ State Key Laboratory of Power Transmission Equipment Technology, School of Electrical Engineering, Chongqing University, Chongqing 400044, China

² Xi'an XD Transformer Co., Ltd., Xi'an 710077, China

* Correspondence: 20191101376@cqu.edu.cn

Abstract: As the imbalance between power demand and load capacity in electrical systems becomes increasingly severe, investigating the temperature variations in transformers under different load stresses is crucial for ensuring their safe operation. The thermal analysis of converter transformers poses challenges due to the complexity of model construction. This paper develops a full-scale model of a converter transformer using a multi-core high-performance computer and explores its thermal state at 80%, 100%, and 120% loading ratios using the COUPLED iteration method. Additionally, to validate the simulation model, 24 FBGs are installed in the experimental transformer to record the temperature data. The results indicate a general upward trend in winding the temperature from bottom to top. However, an internal temperature rise followed by a decrease is observed within certain sections. Moreover, as the loading ratio increases, both the peak temperature and temperature differential of the transformer windings rise, reaching a peak temperature of 107.9 °C at a 120% loading ratio. The maximum discrepancy between the simulation and experimental results does not exceed 3.5%, providing effective guidance for the transformer design and operational maintenance.

Keywords: transformer; full-scale; multiphysics coupled; loading ratio; temperature characteristic



Citation: Yang, F.; Gao, S.; Wang, G.; Hao, H.; Wang, P. Full-Scale Modeling and FBGs Experimental Measurements for Thermal Analysis of Converter Transformer. *Sensors* **2024**, *24*, 3071. <https://doi.org/10.3390/s24103071>

Academic Editor: Nélia J. Alberto

Received: 11 March 2024

Revised: 24 April 2024

Accepted: 9 May 2024

Published: 12 May 2024



Copyright: © 2024 by the authors. Licensee MDPI, Basel, Switzerland. This article is an open access article distributed under the terms and conditions of the Creative Commons Attribution (CC BY) license (<https://creativecommons.org/licenses/by/4.0/>).

1. Introduction

As a pivotal component in power transmission, the converter transformer plays an immensely crucial role, representing one of the most expensive and vital assets within the electrical power system [1]. The operational stability and reliability of a transformer are directly connected to the overall health of the power grid [2]. The hotspot temperature within the windings is a key factor affecting the transformer's load capacity and service life. Excessively high temperatures can lead to insulation aging and winding deformation, subsequently causing broader faults [3]. With the rapid growth in electrical grid load, the construction of transmission and distribution systems cannot always meet the demand promptly, necessitating that transformers inevitably endure varying degrees of loading stress [4]. Therefore, investigating the temperature characteristics of transformers under different loads is of paramount necessity.

The issue of the temperature rise in transformers is primarily governed by the dynamic equilibrium between heating and cooling. Electromagnetic losses constitute the main source of heat [5], while eddy current losses and additional stray losses exacerbate this condition [6]. During normal operation, the maximum temperature in the windings can exceed 80 °C [7], with temperature rises surpassing 40 °C, and a bidirectional coupling relationship exists between electromagnetic losses and temperature [8]. Transformer oil facilitates cooling through continuous circulation, with the cooling effectiveness significantly influenced by the oil flow rate [9], as well as the size and structure of the oil channels [10], which directly relate to the hotspot temperature and its distribution within the transformer. Moreover, the operational environment and the loading ratio [11] of the transformer also exert substantial impacts on the hotspot temperature.

Current research on transformer hotspot temperatures primarily focuses on computational methodologies. On the one hand, 2D or simpler 3D models [12–14], along with tools like Simulink, are utilized to establish the electrothermal equivalent models [15] for calculating hotspot temperature. Comparisons between 2D and 3D modeling approaches have revealed significant inaccuracies associated with 2D models [16]. On the other hand, the most prevalent Computational Fluid Dynamics (CFD) techniques and various hybrid finite element methods [17–19] are employed to analyze and predict transformer hotspot temperatures and diagnose faults. However, these approaches require considerable time for modeling and mesh division, heavily depend on hardware capabilities, take long to solve, and consume substantial operational memory. To address this issue, some researchers have adopted combined 1D–3D modeling [20] techniques or have simplified the modeling analysis by focusing only on certain structures [21]. Additionally, neural networks [22], IoT sensor data [23], and thermal lattice network modeling [24] are alternatives for analyzing hotspot temperatures. Nonetheless, these methodologies cannot comprehensively represent the thermal characteristics of transformers.

Current studies on transformer hotspot temperatures mainly utilize PT100 temperature sensors and Fiber Optic sensors (FOS) [25–28], likely due to cost considerations. Fiber Bragg Grating sensors (FBGs), although more expensive, offer higher accuracy, better electrical insulation, and stronger resistance to interference [29–31]. Ruan et al. employed six FOS to measure the hotspot temperatures of a 10 kV transformer. However, due to the limited number of sensors, the results were not able to fully reflect the characteristics of the temperature distribution [32]. Raza et al. utilized FOS to analyze the temperature rise conditions under various loads for an 11 kV ONAN distribution transformer, obtaining trends of temperature changes under different loads. Nevertheless, their loading durations were short and might not fully represent the actual operating conditions of the transformer [25].

In summary, existing research has provided valuable insights into the temperature distribution in electrical transformers. However, most studies are based on 2D or simplified 3D models, which require enhanced accuracy, and there is a lack of comprehensive research on the hotspot temperatures in converter transformers under various loading ratios using FBGs. To address the aforementioned issues, this article initially employs a fully implicit, bidirectional, pressure-based COUPLED method to investigate the dynamic coupling relationship between thermal and flow aspects in transformers. Subsequently, leveraging real data from a 35 kV oil-immersed scaled-down converter transformer, it establishes an accurate 1:1 3D full-scale model to simulate temperature distribution under various loads. Finally, a transformer testing platform is constructed, and a complete temperature rise test is conducted. Data recorded by 24 FBG units validate the simulation results. The findings offer valuable references for hotspot temperature analysis and prediction in converter transformers under different operational conditions and serve as a guide for improving transformer insulation design methodologies.

The organization of this paper is as follows: Section 2 describes the multiphysics coupled model. Section 3 presents the simulation results of the highest temperatures under three different loading ratios using the 3D model. Section 4 details the construction of the experimental platform for a 35 kV scaled-down converter transformer and the arrangement of FBGs, providing a thorough comparison between the simulation outcomes and experimental results. Finally, Section 5 summarizes the work presented in this paper.

2. Methodology

During the operation of a transformer, the rated current passing through the windings generates a magnetic field that induces electromagnetic losses in the windings and structural components, constituting a primary heat source for the transformer [33]. The Ohmic losses produced by the windings lead to a temperature increase, which, in turn, is further constrained by the generated heat, directly affecting the winding losses.

$$P_{\Omega} = \sum_{e=1}^N \frac{N^2 I^2}{S^2 \sigma} S_e \quad (1)$$

where P_{Ω} is the ohmic loss; e is each mesh unit after finite element analysis; N is the number of winding turns; I is the current; S is the winding area in the model; S_e is the unit area, and σ is the temperature-dependent electrical conductivity of the winding (S/m), expressed as $\sigma = 108-24,545 T$.

Heat dissipation primarily occurs through natural convection, enabled by the oil's thermal buoyancy, creating diverse temperature zones within the converter transformer. As the Mach number of the insulating oil is minimal, the oil is characterized as incompressible. Under steady-state conditions, the fundamental equations that describe the conservation of mass, momentum, and energy are outlined below.

Mass Conservation Equation:

$$\frac{\partial \rho}{\partial t} + \frac{\partial(\rho u)}{\partial x} + \frac{\partial(\rho v)}{\partial y} + \frac{\partial(\rho w)}{\partial z} = 0 \quad (2)$$

Momentum Conservation Equation:

$$\frac{\partial(\rho u)}{\partial t} + \text{div}(\rho u u) = -\frac{\partial \rho}{\partial x} + \frac{\partial \tau_{xx}}{\partial x} + \frac{\partial \tau_{yx}}{\partial y} + \frac{\partial \tau_{zx}}{\partial z} + F_x \quad (3)$$

$$\frac{\partial(\rho v)}{\partial t} + \text{div}(\rho v u) = -\frac{\partial \rho}{\partial y} + \frac{\partial \tau_{xy}}{\partial x} + \frac{\partial \tau_{yy}}{\partial y} + \frac{\partial \tau_{zy}}{\partial z} + F_y \quad (4)$$

$$\frac{\partial(\rho w)}{\partial t} + \text{div}(\rho w u) = -\frac{\partial \rho}{\partial z} + \frac{\partial \tau_{xz}}{\partial x} + \frac{\partial \tau_{yz}}{\partial y} + \frac{\partial \tau_{zz}}{\partial z} + F_z \quad (5)$$

Energy Conservation Equation:

$$\frac{\partial(\rho T)}{\partial t} + \text{div}(\rho u T) = \text{div}(\lambda \text{grad} T) + S_T \quad (6)$$

where x, y, z are the coordinates; u is the x-speed; v is the y-speed; w is the z-speed; ρ is the fluid density; F_x is the x-force density; F_y is the y-force density; F_z is the z-force density; μ is the dynamic viscosity; C_p is the specific heat capacity at constant pressure; λ is the thermal conductivity; T is the temperature; S_T is the heat source (iron losses and winding losses).

The pressure-based, fully implicit COUPLED algorithm enables the simultaneous solution of continuity equations for both momentum and pressure. This is achieved through implicit discretization of the pressure gradient and mass flux across surfaces within the momentum equations. Compared to the segregated algorithm, which employs a semi-implicit approach for separate solutions, the COUPLED algorithm exhibits enhanced performance, achieving faster convergence and higher precision. All physical fields are solved using transient solvers, with the field-dependent material properties updated every time in advance.

3. Model Description

3.1. Full-Scale Model

The research subject of this paper is a 35 kV (800/35-10.5) oil-immersed single-phase scaled-down converter transformer (China XD Group Co., Ltd. Xi'an, China. The version of software: Ansys 17.0). Figure 1 illustrates its full-scale 3D model, which includes the core, windings, insulating cardboard, structural components, and the oil tank. The insulating cardboard encompasses end corner rings, coil insulation, support bars, and oil duct barriers. The oil tank dimensions are 1.6 m (x) \times 0.7 m (y) \times 1.1 m (z), with the HV winding standing 396 mm tall and the LV winding at 442 mm. The tank wall has a thickness of 10 mm. There are four outlets and inlets at the top and bottom of the oil tank, respectively. The materials used for the core, windings, KI50X transformer oil, and T4 insulating cardboard in this platform are the same as those used in the ± 800 kV converter transformers. To ensure similar electrical characteristics, the design utilized scaling formulas from reference [34]. Table 1 lists some parameters of the transformer.

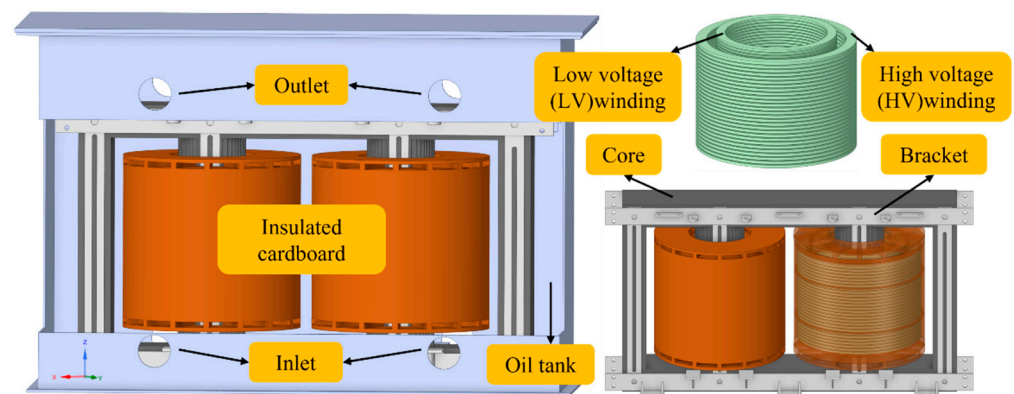


Figure 1. Model configuration.

Table 1. Detailed information of the transformer.

Parameter	Value	Parameter	Value
Capacity (kVA)	800	Core diameter (mm)	210
Frequency (Hz)	50	Core window height (mm)	640
Cooling method	ONAN	HV winding turns	2×440
Voltage level (kV)	35/10.5	LV winding turns	2933
HV rated current (A)	11.43	LV rated current (A)	76.2
HV connection mode	Parallel	LV connection mode	Series

3.2. Fundamental Parameters and Boundary Conditions

The transformer employs an ONAN (Oil Natural Air Natural) cooling method, indicating that the transformer oil circulates via the principle of density differences without external force assistance. Specifically, the heat dissipated by the windings causes the oil temperature to rise and its density to decrease, prompting the oil to flow upward gradually. After cooling in the radiator from the tank's outlet, the oil re-enters the tank through the bottom inlet to recommence the cycle. Consequently, considering the transformer oil's nonlinear material properties as they vary with temperature is essential. Table 2 lists some material parameters, taking into account their nonlinear variation.

Table 2. Fundamental parameters.

Material	Parameter	Values
Insulation oil	Density ρ (kg/m ³)	1098.72–0.712 T
	Coefficient of thermal conductivity λ (W/m·K)	$0.1509-7.01 \times 10^{-5} T$
	Heat capacity at unwavering pressure c_p (J/kg·K)	$1745 + 4.2 T$
	Dynamic viscosity μ (Pa·s)	$0.085-4 \times 10^{-4} T + 5 \times 10^{-7} T^2$
Iron core	Density ρ (kg/m ³)	7650
	Coefficient of thermal conductivity λ (W/m·K)	0.1306
	Heat capacity at unwavering pressure c_p (J/kg·K)	1890
Windings	Heat capacity at unwavering pressure (J/kg·K)	$376.98-3.2 \times 10^{-4} T^2 + 0.221 T$
	Coefficient of thermal conductivity (W/m·K)	$404.18 + 8.64 \times 10^{-5} T^2 - 0.104 T$
	Density ρ (kg/m ³)	8900
	Coefficient of thermal conductivity λ (W/m·K)	338
	Heat capacity at unwavering pressure c_p (J/kg·K)	390
Insulation paperboards	Density ρ (kg/m ³)	1200
	Coefficient of thermal conductivity λ (W/m·K)	0.03
	Heat capacity at unwavering pressure c_p (J/kg·K)	2000

To mimic the thermal state, the transformer windings are evenly divided into multiple sections, and it utilizes coil spacers and oil duct barriers to generate directed passes.

Specifically, the HV winding is divided into four passes, while the LV winding is divided into five passes. This is because the LV side experiences higher currents and temperatures, necessitating more directed sections for effective heat dissipation.

The ambient temperature is set at 17 °C, and a defined heat transfer coefficient is applied to the oil tank to simulate the heat convection of air. The inlet oil velocity is kept constant, and an average pressure condition is established at the domain outlet with no additional pressure applied. Additionally, all solid surfaces are configured with a no-slip condition when in contact with the fluid, as shown in Figure 2.

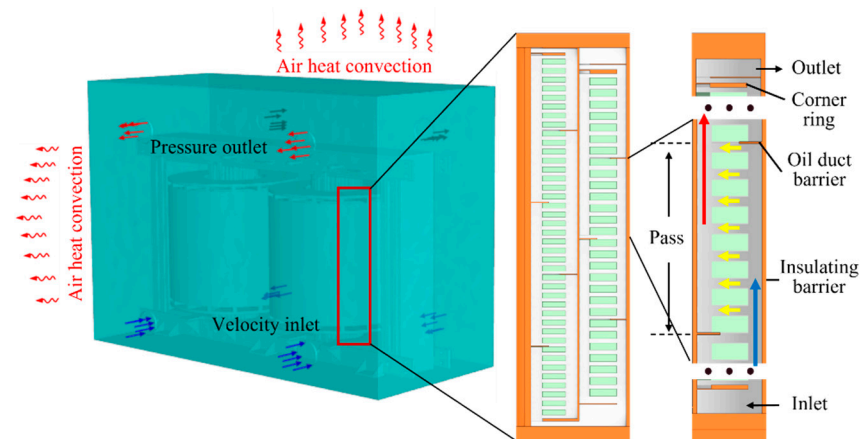


Figure 2. Directed pass configuration.

3.3. Mesh Division

To mimic the full-scale transformer, a multi-scale meshing method is adopted. This study utilizes a hexahedral meshing method, as illustrated in Figure 3. Given that the thickness of the oil duct barriers in the model is only 2 mm, significantly smaller than the dimensions of other components, using a fine mesh would result in an excessive number of elements, imposing computational strain. Conversely, using larger mesh sizes could lead to distortion at the junctions between the oil ducts and windings, severely compromising simulation accuracy. Therefore, we adopt a multi-region decomposition meshing strategy, applying targeted refinement and sweeping treatment at the junctions to enhance mesh density strategically, ensuring a smoother transition between different components.

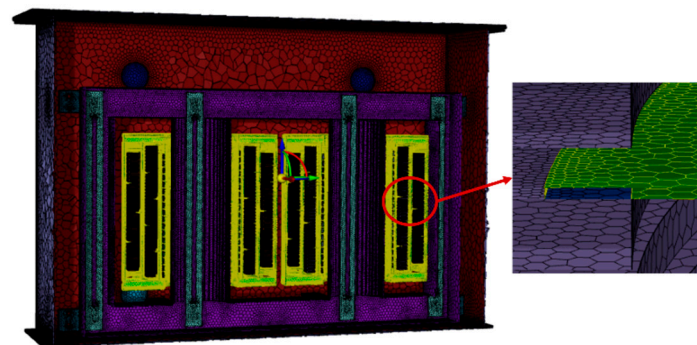


Figure 3. Meshing of full-scale transformer model.

This study performs its computations on a server equipped with 2×64 -core CPUs, operating at a frequency of 3.6 GHz and possessing a memory capacity of 352 GB. To ensure the mesh precision is sufficient to meet computational requirements, various meshing strategies with 13 million, 17 million, and 20 million nodes were tested. It was found that an insufficient number of mesh nodes could lead to significant computational errors. However, the discrepancy in the final temperature field results between the 17 million and

20 million nodes was merely 0.3 °C; thus, the meshing strategy with 17,130,871 nodes was ultimately selected. The quality of the mesh is depicted in Figure 4.

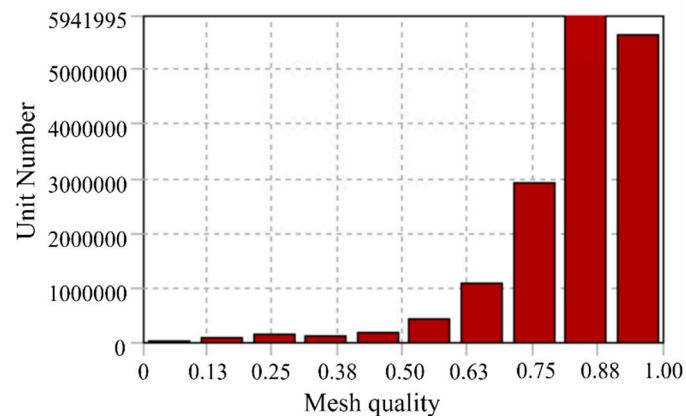


Figure 4. Mesh quality.

4. Simulation Results and Discussion

To investigate the temperature rise characteristics of transformer windings under different loading ratios, this study examined three specific loading conditions: 80%; 100%; and 120%. In addition, detailed analyses were conducted on the temperature distribution along the axial sections and the top circumference in a steady state. The positions of the data points are illustrated in Figure 5, with points A, B, C, and D located on the HV winding and points E, F, G, and H on the LV winding, each set distributed at 90-degree intervals. The axial positions are represented as Line1 and Line2.

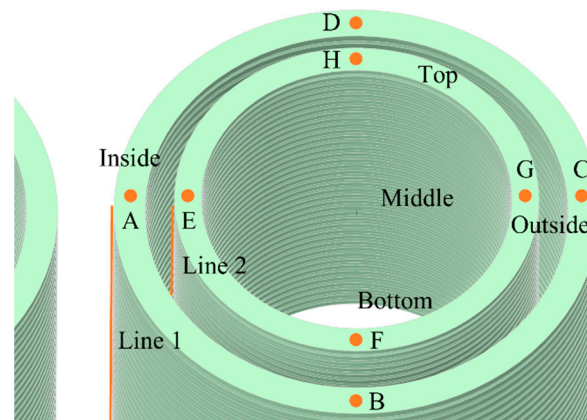


Figure 5. Sampling points of windings.

4.1. Axial Direction Temperature

The axial temperature distribution of the windings is depicted in Figure 6. On the one hand, the temperature field distributions for both the HV and LV windings generally exhibit an upward trend from bottom to top. This is influenced by the oil flow cooling effect; as the temperature rises, the oil flows upward, causing the temperature difference between the winding and the oil to gradually decrease, thereby affecting the heat dissipation. On the other hand, given that the radial width of the main channel around the winding is much greater than the axial height between the coil spacers, the oil flow rate increases in narrower channels under a fixed total oil flow. When the oil duct barrier redirects the flow, the speed increases below the barrier, enhancing the cooling effect, and then slows down after passing the barrier. Consequently, within each section of the winding, the temperature change exhibits an initial increase followed by a decrease.

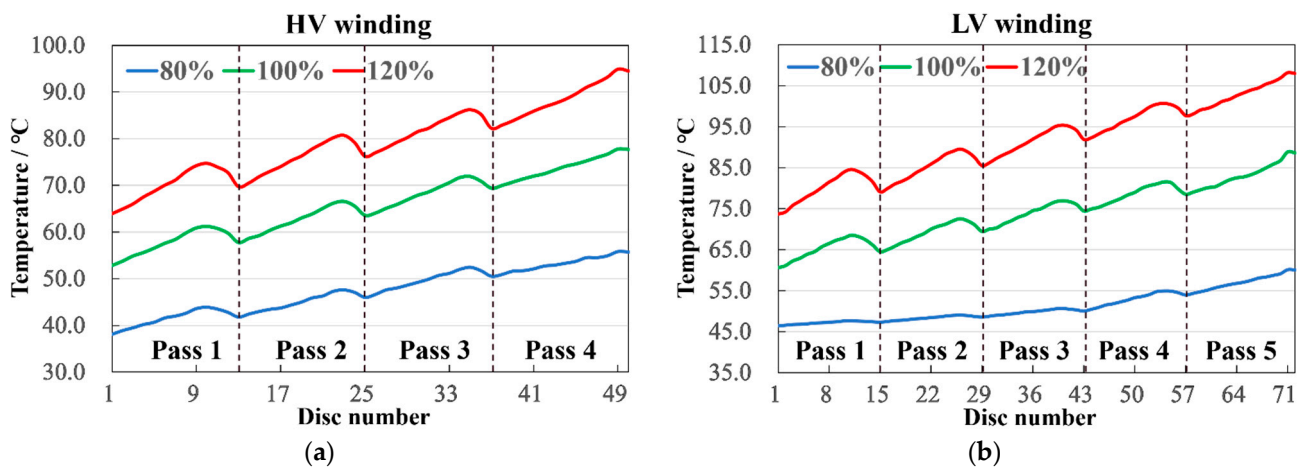


Figure 6. Temperature of every pass. (a) HV winding; (b) LV winding.

For instance, at a 120% loading ratio, as shown in Figure 6a, within pass 1 of the HV winding, the temperature first increases by 10.5 °C, then drops by 4.6 °C; for pass 2, the rise is 10.1 °C, and the fall is 4 °C; for pass 3, the ascent is 9.6 °C, and the descent is 3.6 °C; for pass 4, the increase is 11 °C, and the decrease is 0.8 °C. Concurrently, as shown in Figure 6b, in the LV winding, pass 1 records an 11.2 °C increase and a 6.7 °C decrease; pass 2 shows a 10 °C rise and a 5.5 °C fall; pass 3 has a 9.6 °C elevation and a 4.7 °C reduction; pass 4 undergoes an 8.1 °C increment and a 3.9 °C decrement; pass 5 experiences a 10.3 °C upturn and a 0.6 °C downturn.

Comparing the results across the three loading ratios reveals that with an increase in loading ratio, the magnitude of temperature rise and fall within each section also grows, but the temperature difference within the same winding's different sections decreases. This phenomenon suggests that a higher loading ratio leads to higher temperatures, thereby increasing the flow rate and improving the cooling effect. However, when the flow rate is constant, the cooling effect gradually weakens with rising temperatures. Additionally, it is observed that the temperature drop in the terminal sections is very slight. Structurally, this is because the terminal sections, or the top positions of the windings, are encased by multiple corner rings, resulting in minor flow speed changes when the oil passes through barriers, hence the subtle temperature variation.

4.2. Radial Direction Temperature

The radial temperature distribution at the top of the windings is depicted in Figure 7. The diagram illustrates that the temperature varies circumferentially for each coil disc, decreasing gradually from the inside to the outside. Specifically, the temperatures at points A and E are notably higher than those at other points on the circumference; the temperatures at points B, D, F, and H are relatively low and similar, marking the lowest temperature points, while the temperatures at points C and G are intermediate. This pattern occurs because the heat sources are relatively concentrated, and the cooling conditions are poorer at the positions adjacent to the two-column windings, resulting in higher temperatures. The external positions have slightly less heat source and notably better cooling conditions than the internal ones. The least heat is at points B, D, F, and H, which only emanate heat from the windings themselves and are almost unobstructed, thereby having optimal cooling conditions and the lowest temperatures.

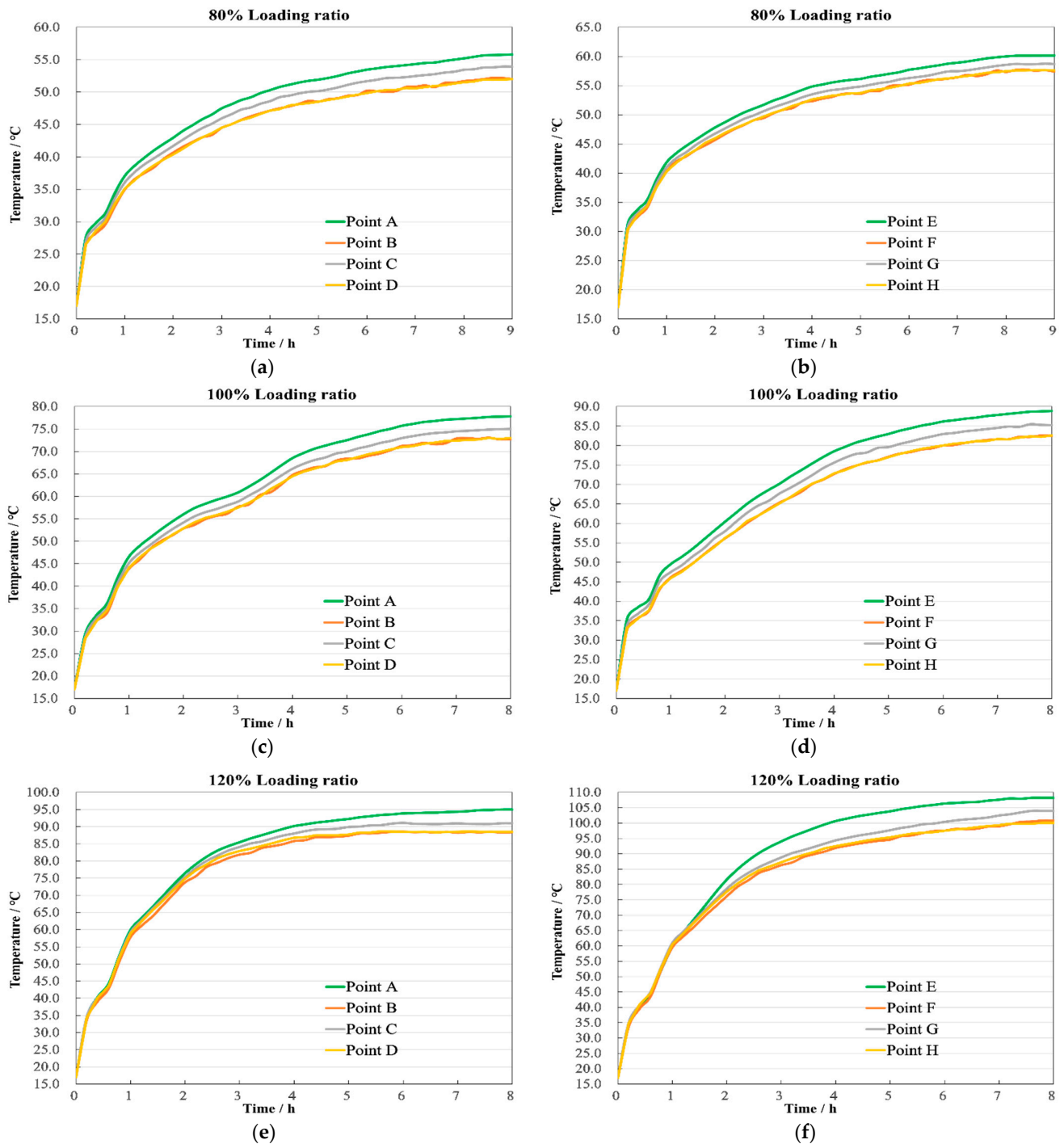


Figure 7. Winding end temperature. (a) 80% HV winding; (b) 80% LV winding; (c) 100% HV winding; (d) 100% LV winding; (e) 120% HV winding; (f) 120% LV winding.

Moreover, it is observed that the temperature differential around the circumference increases with the loading ratio. At an 80% loading ratio, as shown in Figure 7a,b, the maximum temperature difference is 3.9 °C for the HV winding and 4.2 °C for the LV winding; at a 100% loading ratio, as shown in Figure 7c,d, they are 5.8 °C and 6.3 °C, respectively; and at a 120% loading ratio, as shown in Figure 7e,f, they are 8.3 °C and 9.1 °C, respectively. However, the variations between points B, D, F, and H become increasingly minor. These observations indicate that the impact of cooling conditions intensifies with the rising temperature. Yet, when the cooling conditions are constant, the higher the temperature, the lesser the impact becomes.

4.3. Temperature Distribution

Through this research, we have identified the locations of the highest temperatures within the windings. Subsequently, we analyze the change patterns and distribution characteristics of the highest temperatures over time. Figure 8 displays the steady-state temperature distribution of the windings when the transformer operates at an 80% loading ratio. It reveals that the highest temperature at the top of the LV winding is 60.2 °C, while at the HV winding top, it is 55.8 °C, with a temperature difference of 4.4 °C. The overall temperature distribution across the windings is relatively uniform, with minor temperature differences between the sections. This uniformity results from the lower losses and temperature rises associated with the smaller loading ratio, coupled with the slower oil flow rate, which yields more gradual and even temperature changes.

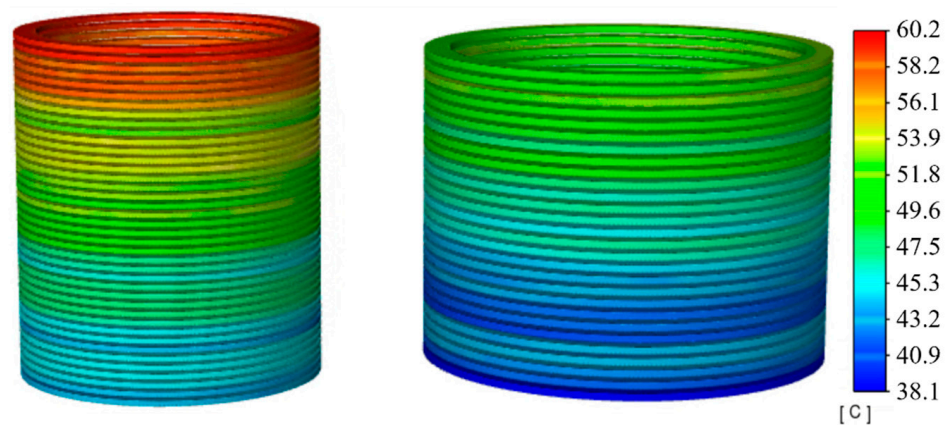


Figure 8. Temperature contour with 80% load.

Figure 9 illustrates the temperature change curves per hour at the top, middle, and bottom positions of the windings. Initially, the temperature change rate of the LV winding is greater than that of the HV winding. Subsequently, the temperature rise in both windings slows down, reaching a steady state near 8 h of operation. The temperature differences at the top, middle, and bottom of the HV winding are 7.7 °C and 9.5 °C, respectively, as shown in Figure 9a, while for the LV winding, they are 10.2 °C and 3.3 °C, as shown in Figure 9b. The LV winding, positioned between the core and HV winding, exhibits inferior cooling conditions compared to the HV winding. Additionally, with the oil at the bottom being cooler and the flow being relatively slow, the temperature rise differences between the middle and bottom are marginal.

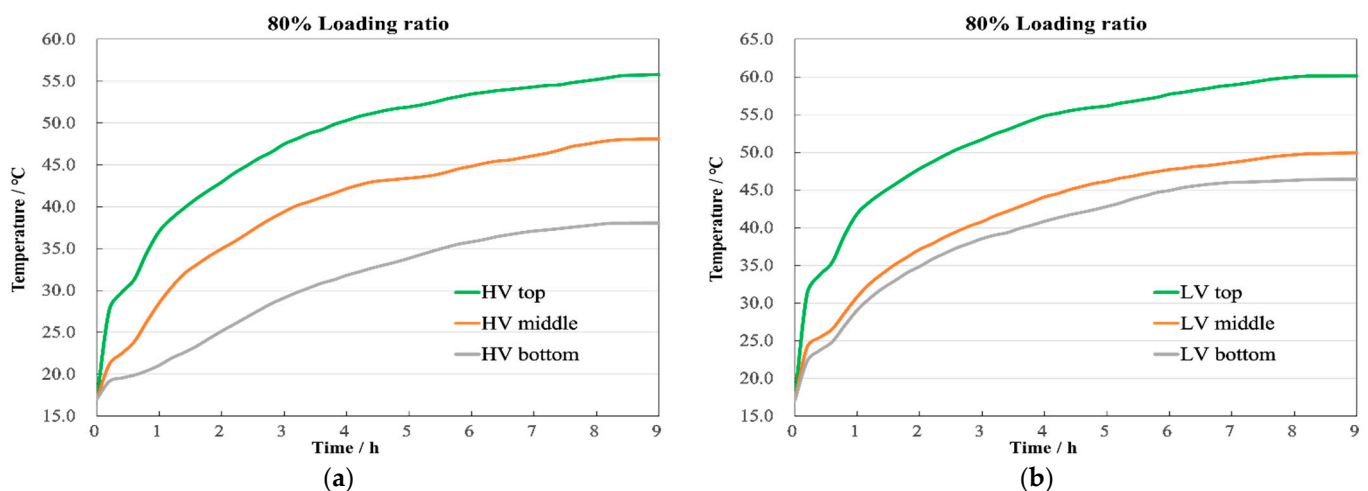


Figure 9. Axial temperature with 80% load. (a) HV winding; (b) LV winding.

At a 100% loading ratio or rated operating condition, the highest temperature for the LV winding reaches 88.6 °C, and for the HV winding, it is 77.8 °C, showing a difference of 10.8 °C, as illustrated in Figure 10. Compared to the 80% loading ratio condition, increased losses lead to higher temperature rises and quicker oil flow, making the temperature change process due to oil flow direction and speed more evident across different sections.

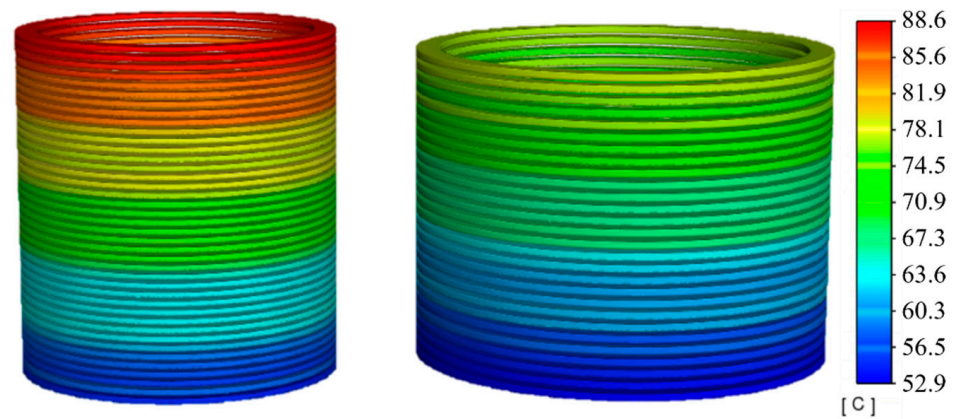


Figure 10. Temperature contour with 100% load.

From the temperature change curves in Figure 11, it is evident that, compared to an 80% loading ratio, the initial temperature rise rate at a 100% loading ratio has significantly increased, with the temperatures stabilizing around 7 h, reducing the time by 52 min. The temperature differences at the top, middle, and bottom of the HV winding are 11.1 °C and 13.9 °C, respectively, as shown in Figure 11a, similar to those in the LV winding, which are 13.1 °C and 14.9 °C, as shown in Figure 11b, demonstrating a regular temperature distribution during rated operation.

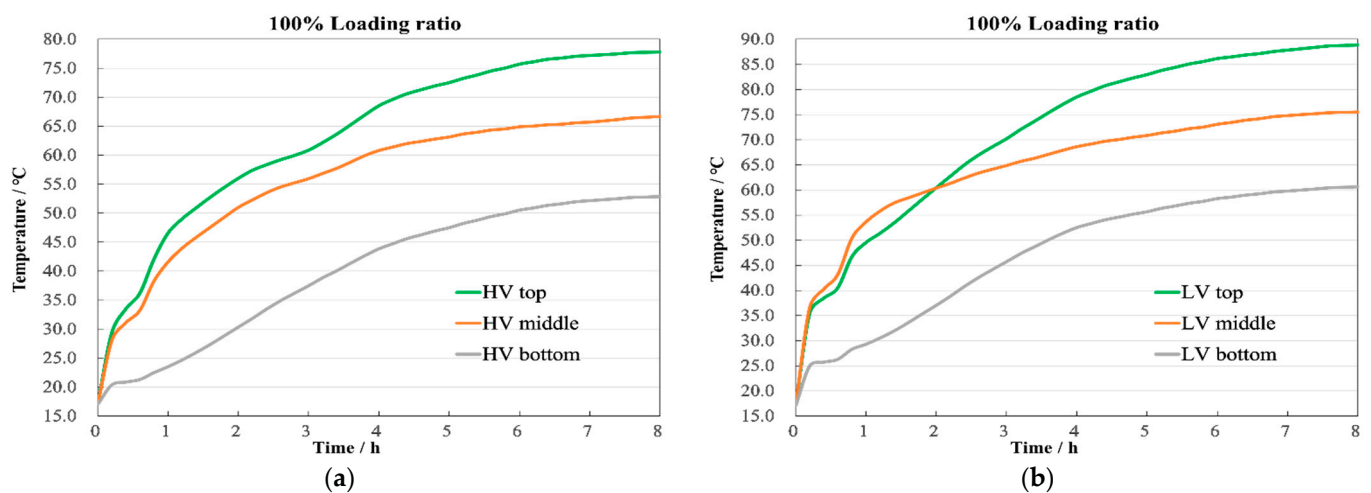


Figure 11. Axial temperature with 100% load. (a) HV winding; (b) LV winding.

At a 120% loading ratio, an overload condition, Figure 12 shows a marked increase in overall winding heat generation compared to normal operating conditions, with distinct temperature changes between adjacent sections. This indicates that the higher the temperature, the more pronounced the cooling effect changes due to flow speed. At this point, the highest temperature for the LV winding reaches 108.2 °C, and for the HV winding, it is 94.9 °C, a difference of 13.3 °C.

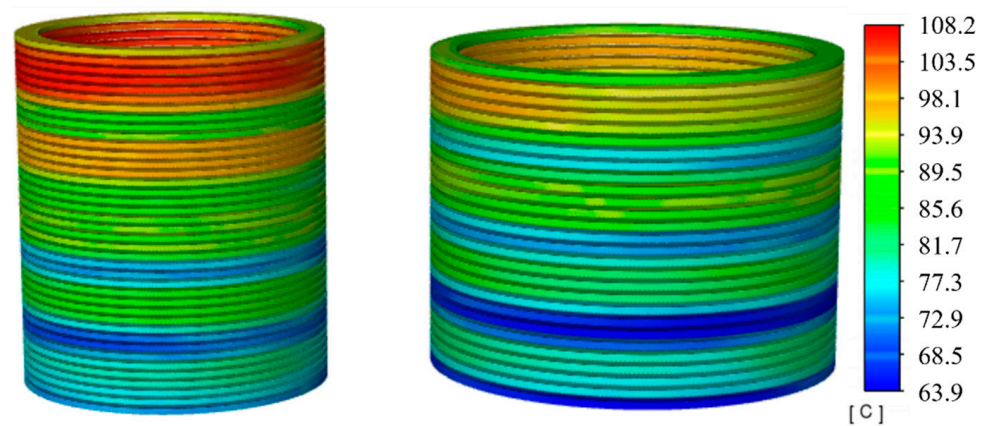


Figure 12. Temperature contour with 120% load.

These changes are well illustrated in Figure 13. With the increase in loading ratio, the rate of temperature rise in the windings further accelerates, reaching a steady state near 6 h, which is 76 min faster than under normal conditions. The temperature differences at the top, middle, and bottom of the HV winding are 14.7 °C and 16.3 °C, respectively, as shown in Figure 13a, while in the LV winding, they are 15.8 °C and 18.7 °C, as shown in Figure 13b.

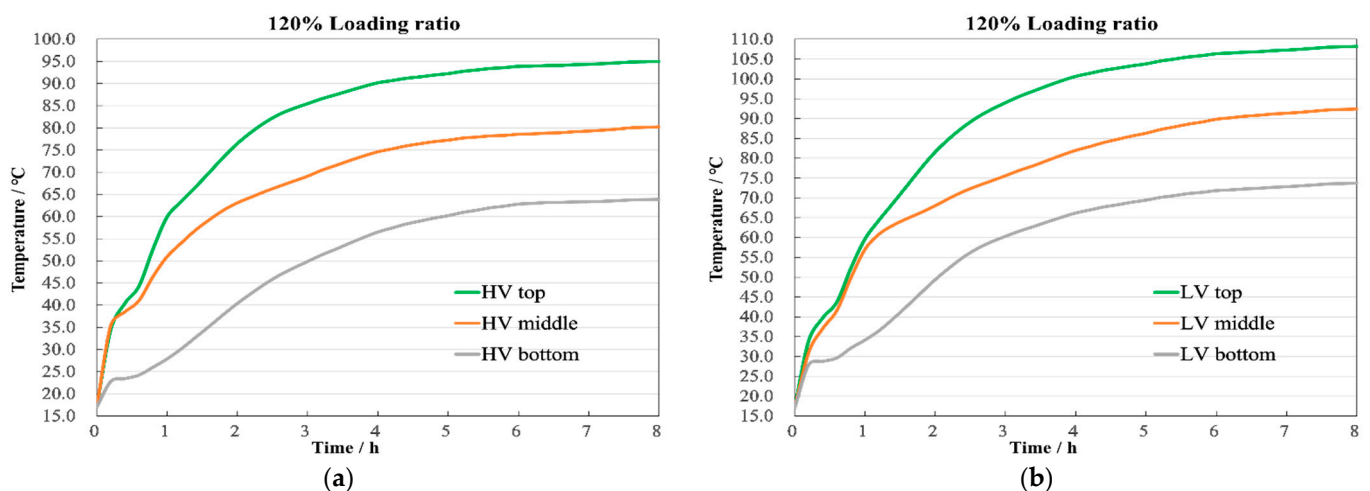


Figure 13. Axial temperature with 120% load. (a) HV winding; (b) LV winding.

5. Temperature Rise Test and Analysis

5.1. Construction of Experimental Platform

To verify the accuracy of the aforementioned computational results, we established an experimental platform for a 35 kV single-phase scaled-down converter transformer and positioned the corresponding sensors within the windings to monitor temperature changes. Despite the higher cost of FBGs, to ensure the reliability of the experimental results, we chose 24 of the most representative points for measurement based on previous calculations and placed the FBGs at the top, middle, and bottom parts, installing four sensors evenly around the circumference of each coil, as shown in Figure 14.

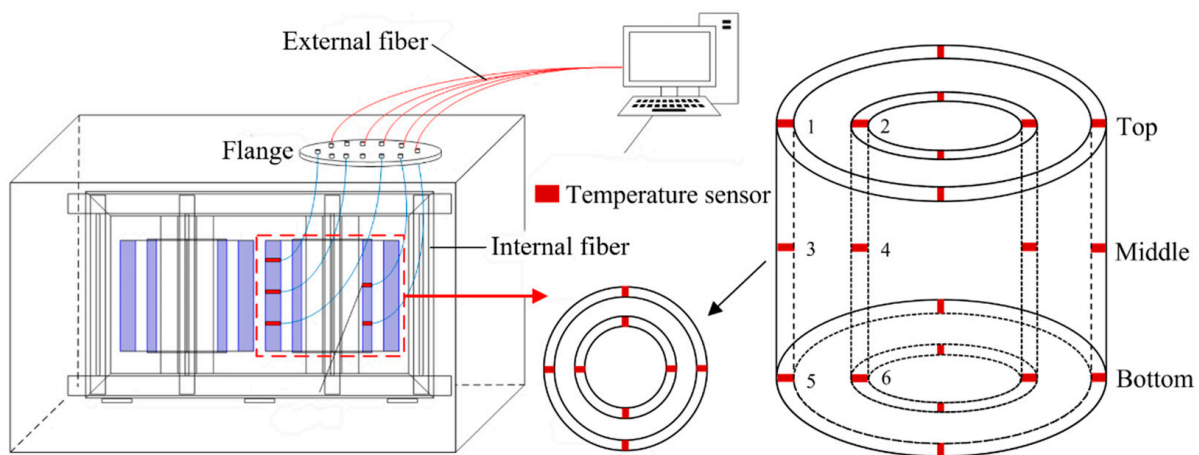


Figure 14. Sensor arrangement options.

FBGs are created by inscribing gratings onto the optical fiber core, which serve as narrow-band reflective filtering elements. The grating causes reflection of a single wavelength while transmitting others. Temperature changes result in variations in the effective refractive index and grating period, thus shifting the reflected wavelength [35]. The FBGs used in this experiment are encapsulated in glass fiber to ensure stable operation, with a wavelength range between 1528 and 1566. They have a temperature collection range from -40 to 180 °C, with a resolution of 0.1 °C and a measurement error of less than ± 1 °C. Considering factors like vibration and temperature that may affect the stability of transmission, to ensure that the FBGs are not damaged due to changes in the spacing between the coils, we have reserved space in the spacers and secured the FBGs within them, as shown in Figure 15a. Moreover, the customized sensors are designed to maintain their measurement precision and ensure the validity of the experimental results. Subsequently, they are connected to a flange on the top of the oil tank through internal optical cables, and external optical cables connect them to smart temperature measurement devices for storing and analyzing temperature data. The overall assembly of the winding containing all sensors is illustrated in Figure 15b.

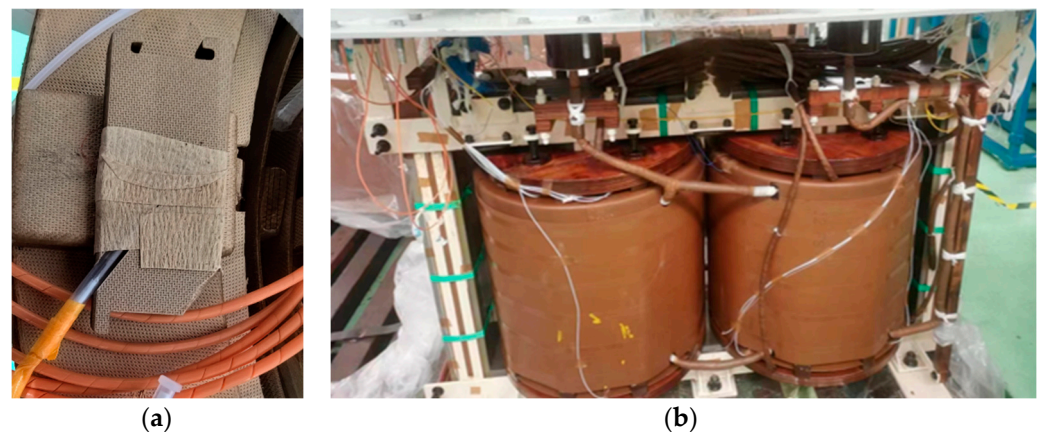


Figure 15. Sensor installation method. (a) FBGs placement (b) Winding with all sensors.

The temperature rise test is one of the most critical routine tests for transformers, assessing the temperature change characteristics of the transformer windings under different operating conditions. It is the most time-consuming test and requires a high-capacity power source for support. Following the guidelines of relevant international standards to ensure the safety of the test procedure, this study employed a short-circuit wiring method, short-circuiting the two low-voltage bushings with a metal plate and connecting the high-voltage

bushing to an AC power source. The power voltage was adjusted according to the loading ratio, and the wiring circuit is shown in Figure 16. The transformer was considered to have reached a steady state when the rate of temperature change at the measuring points was less than $1\text{ }^{\circ}\text{C}/\text{h}$, after which the test was terminated. The test environment was maintained at $17\text{ }^{\circ}\text{C}$, with the experimental platform and site wiring depicted in Figure 17.

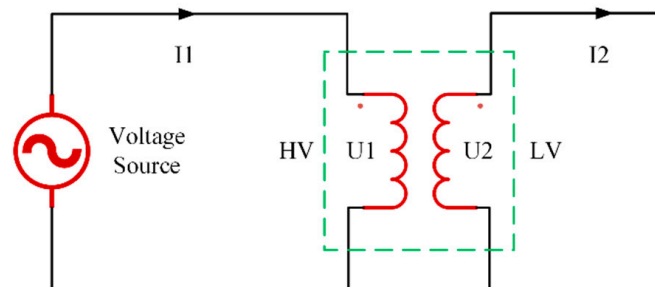


Figure 16. Schematic diagram of the experimental circuit.

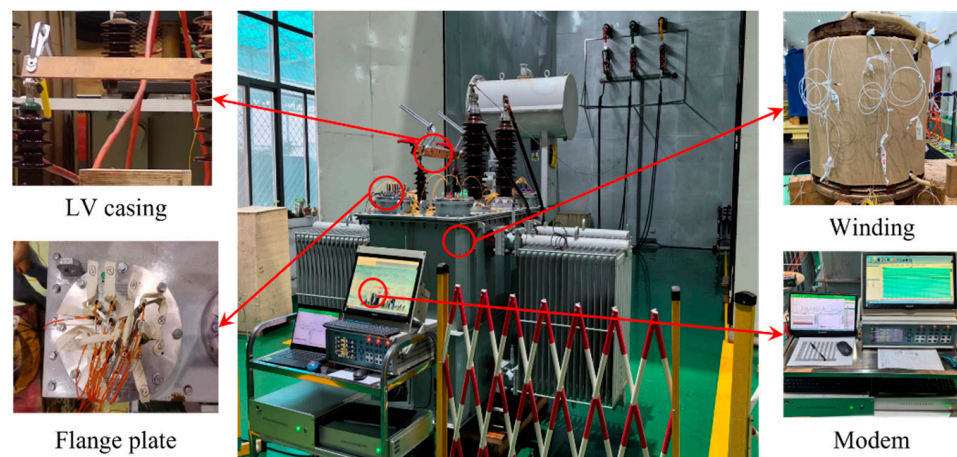


Figure 17. Experimental on-site.

5.2. Experimental Results and Discussion

The experiment was conducted in three sessions, corresponding to 80%, 100%, and 120% loading ratios, respectively. Each test began at room temperature and continued until a steady state was achieved. The transformer was allowed to cool back to room temperature before commencing the subsequent test, with a data recording frequency of once per minute.

5.2.1. Axial Temperature Characteristics

The temperature characteristics over time for the top, middle, and bottom measurement points of the windings are displayed in Figure 18. The first set of experiments at an 80% loading ratio lasted the longest, approximately 9.1 h, with the transformer reaching a steady state at 8 h. At this point, the HV winding temperatures were $53.9\text{ }^{\circ}\text{C}$, $46.28\text{ }^{\circ}\text{C}$, and $36.37\text{ }^{\circ}\text{C}$, respectively, as shown in Figure 18a, while the LV winding recorded $58.35\text{ }^{\circ}\text{C}$, $48.2\text{ }^{\circ}\text{C}$, and $44.78\text{ }^{\circ}\text{C}$, as shown in Figure 18b. Compared to the simulation results, the maximum discrepancy was $1.9\text{ }^{\circ}\text{C}$, located at the top of the HV winding.

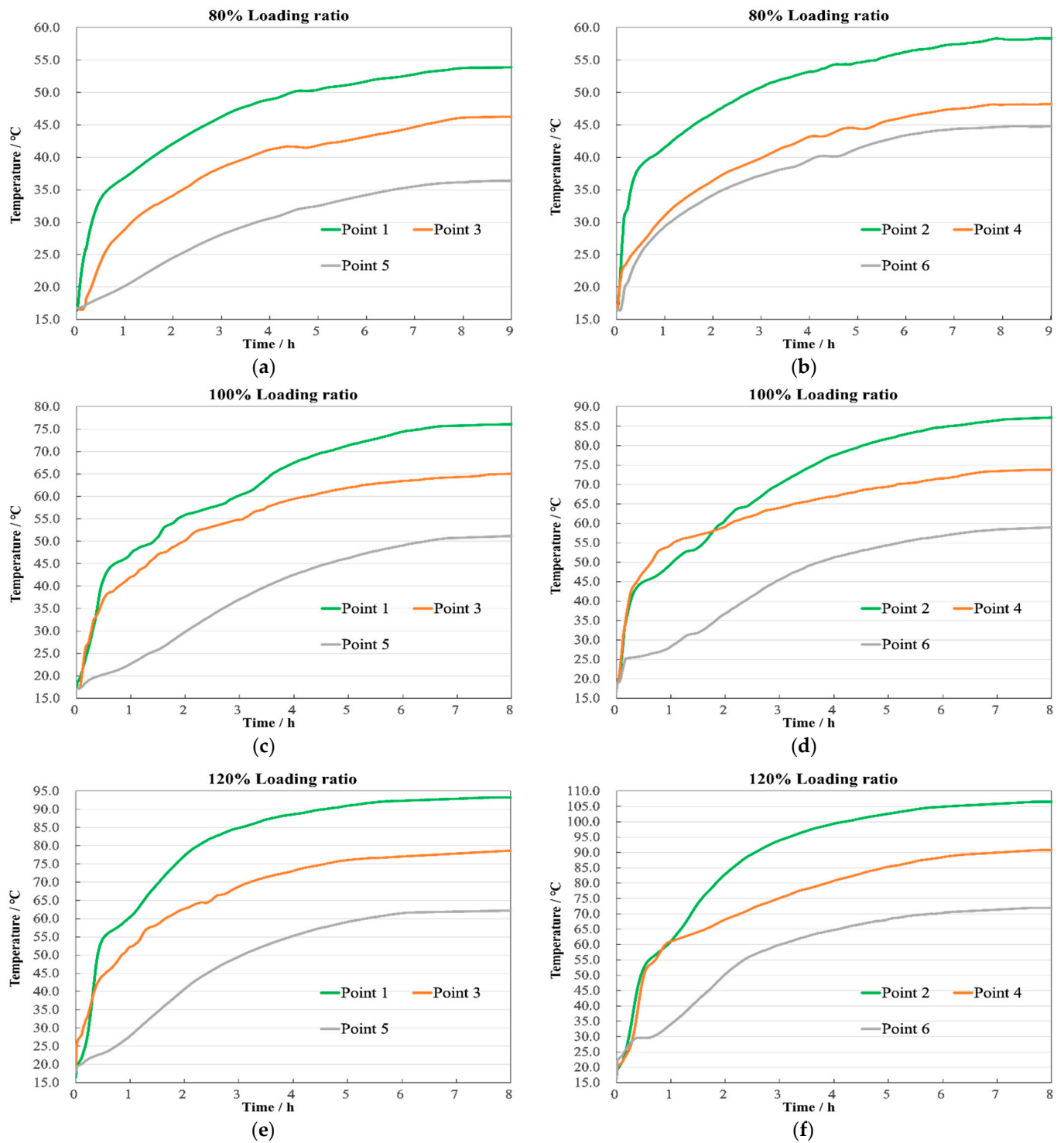


Figure 18. Axial temperature. (a) 80% HV winding; (b) 80% LV winding; (c) 100% HV winding; (d) 100% LV winding; (e) 120% HV winding; (f) 120% LV winding.

The second set of experiments at a 100% loading ratio lasted about 8.3 h, with a steady state achieved around 7.1 h. The temperatures for the HV winding were then 76.11 °C, 65.04 °C, and 51.2 °C, respectively, as shown in Figure 18c. And for the LV winding, they were 87.21 °C, 73.78 °C, and 58.96 °C, as shown in Figure 18d. The largest difference between the experimental and simulation results was 1.73 °C, found in the middle of the LV winding.

The third set at a 120% loading ratio lasted about 7.8 h, reaching the steady state at approximately 5.8 h. The recorded temperatures for the HV winding were 93.23 °C, 78.65 °C, and 62.22 °C, as shown in Figure 18e. And for the LV winding, they were 106.5 °C, 90.77 °C, and 71.98 °C, as shown in Figure 18f. The highest discrepancy compared to the simulation was 1.74 °C at the top of the HV winding.

After the transformer reaches a steady state, the comparison between simulation and experimental temperatures is summarized in Table 3. Furthermore, after comparing the simulation and experimental values at all instances, the maximum discrepancy found was 1.9 °C at the top of the HV winding during the 80% loading rate experiment in steady state, representing an error rate of 4.5%, as shown in Figure 19.

Table 3. Comparison of results.

Loading Ratio	Location	HV Temperature (°C)			LV Temperature (°C)		
		Test	Simulation	Errors	Test	Simulation	Errors
80%	Top	53.90	55.80	1.90	58.35	60.20	1.85
	Middle	46.28	48.10	1.82	48.20	49.94	1.74
	Bottom	36.37	38.06	1.69	44.78	46.43	1.65
100%	Top	76.11	77.80	1.70	87.20	88.60	1.40
	Middle	65.03	66.71	1.67	73.78	75.51	1.73
	Bottom	51.19	52.85	1.66	58.96	60.60	1.64
120%	Top	93.23	94.97	1.74	106.50	108.21	1.71
	Middle	78.65	80.24	1.59	90.77	92.45	1.68
	Bottom	62.20	63.90	1.69	71.98	73.71	1.73

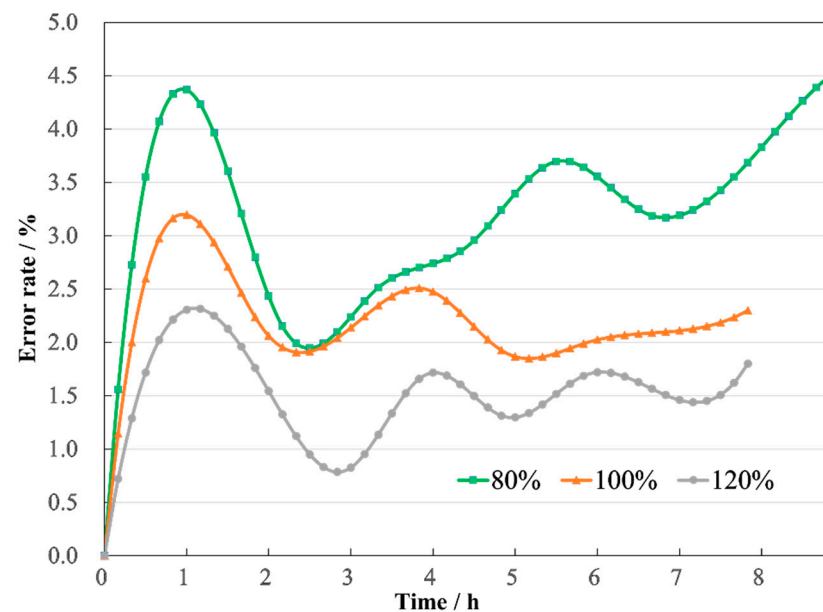


Figure 19. Errors of temperature.

5.2.2. Radial Direction Temperature

The radial temperature distributions for the HV and LV windings under different loading ratios are shown in Figure 19. The temperature along the circumference of the same coil disc decreases from the inside to the outside, with points A and E registering the highest temperatures on the circumference. The pattern of temperature rise at each point is essentially the same, with variations only in the peak values. At an 80% loading ratio, as shown in Figure 20a,b, the maximum temperature difference was 4.3 °C for the HV winding and 4.5 °C for the LV winding; at 100% loading, as shown in Figure 20c,d, they were 6.6 °C and 7.2 °C, respectively; and at 120% loading, as shown in Figure 20e,f,

they were 9.3 °C and 8.5 °C, respectively. This demonstrates that the transformer's highest operating temperature is located at the top of the windings near the position between two adjacent pillar windings. This conclusion applies to almost all transformers. Designers can control the hotspot temperature to stay within safe values by increasing spacing or flow rate. The experimental outcomes effectively validate the accuracy of the simulation results.

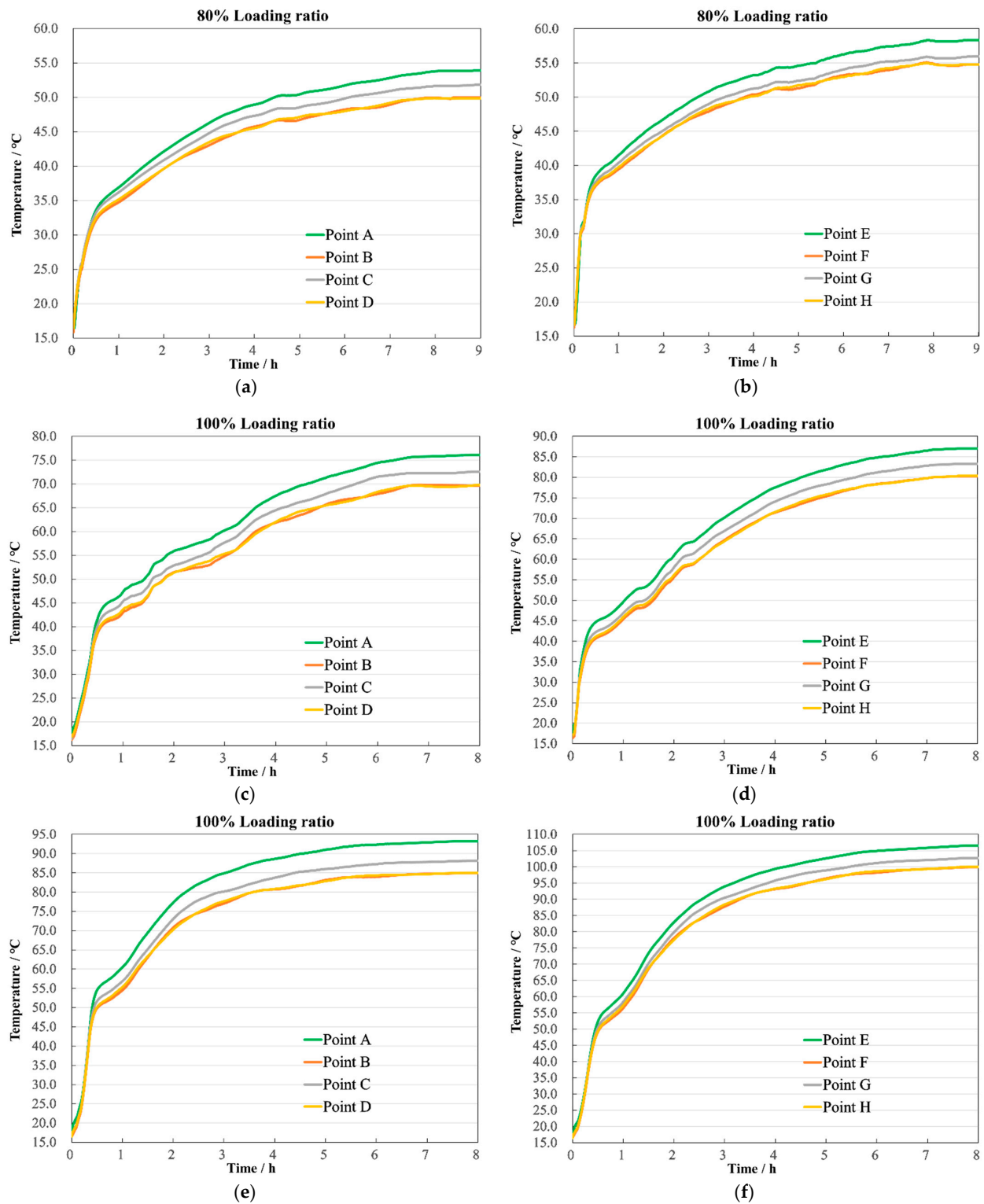


Figure 20. Winding end temperature. (a) 80% HV winding; (b) 80% LV winding; (c) 100% HV winding; (d) 100% LV winding; (e) 120% HV winding; (f) 120% LV winding.

6. Conclusions

This paper established a high-precision 3D model of a 35 kV scaled-down converter transformer and conducted coupled electromagnetic–thermal–fluid calculations under three loading conditions: 80%; 100%; and 120%. The analysis of the winding temperature rise characteristics led to the following conclusions:

- (1) The axial temperature distribution of the windings demonstrates a progressive increase from bottom to top. Significant changes in flow velocity on either side of the oil duct barriers markedly impact the cooling effect, resulting in temperature within each winding section first increasing and then decreasing. The maximum radial temperatures are observed at positions adjacent to the two-column windings, decreasing gradually toward the outer side;
- (2) With increasing loading ratios, the time for the transformer to reach a steady state decreases, but the temperature differences between the HV and LV windings, as well as among the top, middle, and bottom of the windings, increase. At a 120% loading ratio, the maximum temperature can reach 107.9 °C, with the largest temperature difference being up to 35.4 °C;
- (3) The establishment of the full-scale model significantly enhances the precision of simulation calculations. According to the data collected by the FBG sensors, the validation results for the coupled calculation model indicate that the error during the transition from rated operation to steady state is less than 2.3%.

This paper provides valuable guidance for transformer design, temperature prediction, and operational safety.

Author Contributions: Conceptualization, S.G. and H.H.; methodology, all authors; software, S.G.; validation, all authors; investigation, S.G., H.H. and G.W.; resources, F.Y. and G.W.; writing—original draft preparation, S.G. and H.H.; writing—review and editing, F.Y. and P.W.; supervision, G.W.; project administration, F.Y. and P.W.; funding acquisition, F.Y. and G.W. All authors have read and agreed to the published version of the manuscript.

Funding: This research was supported by the National Key Research and Development Program of China (grant numbers 2021YFB2401700).

Institutional Review Board Statement: Not applicable.

Informed Consent Statement: Not applicable.

Data Availability Statement: Data are contained within the article.

Conflicts of Interest: Xi'an XD Transformer Co., Ltd. belongs to the same research unit as Chongqing University in this project, funded by the National Key Research and Development Program of China. We have no conflict of interest with this company.

References

1. Gezezin, C.; Ozgonenel, O.; Dirik, H. A monitoring method for average winding and hot-spot temperatures of single-phase, oil-immersed transformers. *IEEE Trans. Power Deliv.* **2020**, *36*, 3196–3203. [[CrossRef](#)]
2. Xiao, D.; Xiao, R.; Yang, F.; Chi, C.; Hua, M.; Yang, C. Simulation research on ONAN transformer winding temperature field based on temperature rise test. *Therm. Sci.* **2022**, *26 Pt A*, 3229–3240. [[CrossRef](#)]
3. Kebriti, R.; Hossieni, S.M.H. 3D modeling of winding hot spot temperature in oil-immersed transformers. *Electr. Eng.* **2022**, *104*, 3325–3338. [[CrossRef](#)]
4. Ai, M.; Shan, Y. The whole field temperature rise calculation of oil-immersed power transformer based on thermal network method. *Int. J. Appl. Electromagn. Mech.* **2022**, *70*, 55–72. [[CrossRef](#)]
5. Liu, C.; Hao, J.; Liao, R.; Yang, F.; Li, W.; Li, Z. Magnetic flux leakage, eddy current loss and temperature distribution for large scale winding in UHVDC converter transformer based on equivalent 2D axisymmetric model. *Electr. Eng.* **2024**, *106*, 711–725. [[CrossRef](#)]
6. Shiravand, V.; Faiz, J.; Samimi, M.H.; Djamali, M. Improving the transformer thermal modeling by considering additional thermal points. *Int. J. Electr. Power Energy Syst.* **2021**, *128*, 106748. [[CrossRef](#)]

7. Li, L.; Liu, W.; Chen, H.; Liu, X. Prediction of oil flow and temperature distribution of transformer winding based on multi-field coupled approach. *J. Eng.* **2019**, *2019*, 2007–2012. [[CrossRef](#)]
8. Yu, X.; Tan, Y.; Wang, H.; Wang, X.; Zang, Y.; Guo, P. Thermal analysis and optimization on a transformer winding based on non-uniform loss distribution. *Appl. Therm. Eng.* **2023**, *226*, 120296. [[CrossRef](#)]
9. Córdoba, P.A.; Dari, E.; Silin, N. A 3D numerical model of an ONAN distribution transformer. *Appl. Therm. Eng.* **2019**, *148*, 897–906. [[CrossRef](#)]
10. Yuan, F.; Wang, Y.; Tang, B.; Yang, W.; Jiang, F.; Han, Y.; Han, S.; Ding, C. Heat dissipation performance analysis and structural parameter optimization of oil-immersed transformer based on flow-thermal coupling finite element method. *Therm. Sci.* **2022**, *26 Pt A*, 3241–3253. [[CrossRef](#)]
11. Gao, C.; Huang, L.; Feng, Y.; Gao, E.; Yang, Z.; Wang, K. Thermal field modeling and characteristic analysis based on oil immersed transformer. *Front. Energy Res.* **2023**, *11*, 1147113. [[CrossRef](#)]
12. Shiravand, V.; Faiz, J.; Samimi, M.H.; Mehrabi-Kermani, M. Prediction of transformer fault in cooling system using combining advanced thermal model and thermography. *IET Gener. Transm. Distrib.* **2021**, *15*, 1972–1983. [[CrossRef](#)]
13. Ni, R.; Chen, J.; Yang, C.; Li, C.; Qiu, R.; Liu, Z.; Li, R.; Gao, L.; Li, Y. A temperature calculation method of oil immersed transformer considering delay effects and multiple environmental factors. *Electr. Power Syst. Res.* **2022**, *213*, 108260. [[CrossRef](#)]
14. Mikhak-Beyranvand, M.; Faiz, J.; Rezaeealam, B. Thermal analysis and derating of a power transformer with harmonic loads. *IET Gener. Transm. Distrib.* **2020**, *14*, 1233–1241. [[CrossRef](#)]
15. Aslam, M.; Haq, I.U.; Rehan, M.S.; Basit, A.; Arif, M.; Khan, M.I.; Sadiq, M.; Arbab, M.N. Dynamic thermal model for power transformers. *IEEE Access* **2021**, *9*, 71461–71469. [[CrossRef](#)]
16. Daghrah, M.; Zhang, X.; Wang, Z.; Liu, Q.; Jarman, P.; Walker, D. Flow and temperature distributions in a disc type winding-part I: Forced and directed cooling modes. *Appl. Therm. Eng.* **2020**, *165*, 114653. [[CrossRef](#)]
17. Liu, G.; Zheng, Z.; Ma, X.; Rong, S.; Wu, W.; Li, L. Numerical and experimental investigation of temperature distribution for oil-immersed transformer winding based on dimensionless least-squares and upwind finite element method. *IEEE Access* **2019**, *7*, 119110–119120. [[CrossRef](#)]
18. Zhang, X.; Wang, Z.; Liu, Q.; Jarman, P.; Negro, M. Numerical investigation of oil flow and temperature distributions for ON transformer windings. *Appl. Therm. Eng.* **2018**, *130*, 1–9. [[CrossRef](#)]
19. Chi, C.; Gao, B.; Yang, F.; Liao, R.; Cheng, L.; Zhang, L. Investigation on the nonlinear thermal-electrical properties coupling performance of converter transformer. *Appl. Therm. Eng.* **2019**, *148*, 846–859. [[CrossRef](#)]
20. Chi, C.; Yang, F.; Xu, C.; Cheng, L.; Yang, C. A multi-scale thermal-fluid coupling model for ONAN transformer considering entire circulating oil systems. *Int. J. Electr. Power Energy Syst.* **2022**, *135*, 107614. [[CrossRef](#)]
21. Zhang, H.; Liu, G.; Lin, B.; Deng, H.; Li, Y.; Wang, P. Thermal evaluation optimization analysis for non-rated load oil-natural air-natural transformer with auxiliary cooling equipment. *IET Gener. Transm. Distrib.* **2022**, *16*, 3080–3091. [[CrossRef](#)]
22. Bragone, F.; Morozovska, K.; Hilber, P.; Laneryd, T.; Luvisotto, M. Physics-informed neural networks for modelling power transformer's dynamic thermal behaviour. *Electr. Power Syst. Res.* **2022**, *211*, 108447. [[CrossRef](#)]
23. Qu, Y.; Zhao, H.; Zhao, S.; Ma, L.; Mi, Z. Evaluation method for insulation degradation of power transformer windings based on incomplete internet of things sensing data. *IET Sci. Meas. Technol.* **2024**, *18*, 130–144. [[CrossRef](#)]
24. Wang, Y.; Shi, C.; Gao, M.; Xu, Y.; Fu, M.; Zhuo, R. Improved thermal hydraulic network modelling and error analysis in disc-type transformer windings. *IET Gener. Transm. Distrib.* **2024**, *18*, 202–213. [[CrossRef](#)]
25. Raza, S.A.; Ullah, A.; He, S.; Wang, Y.; Li, J. Empirical Thermal Investigation of Oil-Immersed Distribution Transformer under Various Loading Conditions. *CMES-Comput. Model. Eng. Sci.* **2021**, *129*, 829–847.
26. Zhang, Z.S.; Liu, D.; Liu, B.F.; Shi, X.D.; Liu, Z.Q. Temperature of Transformer Controller Based on TMS320C6713. *Adv. Mater. Res.* **2013**, *823*, 555–558. [[CrossRef](#)]
27. Susa, D.; Lehtonen, M.; Nordman, H. Dynamic thermal modeling of distribution transformers. *IEEE Trans. Power Deliv.* **2005**, *20*, 1919–1929. [[CrossRef](#)]
28. Zhao, J.; Wang, H.; Sun, X. Study on the performance of polarization maintaining fiber temperature sensor based on tilted fiber grating. *Measurement* **2021**, *168*, 108421. [[CrossRef](#)]
29. Shi, C.; Ma, G.; Mao, N.; Zhang, Q.; Zheng, Q.; Li, C.; Zhao, S. Ultrasonic detection coherence of fiber Bragg grating for partial discharge in transformers. In Proceedings of the 2017 IEEE 19th International Conference on Dielectric Liquids (ICDL), Manchester, UK, 25–29 June 2017; IEEE: New York, NY, USA, 2017; pp. 1–4.
30. Sarkar, B.; Koley, C.; Roy, N.; Kumbhakar, P. Condition monitoring of high voltage tranModifiedsformers using Fiber Bragg Grating Sensor. *Measurement* **2015**, *74*, 255–267. [[CrossRef](#)]
31. Zhao, Z.Q.; MacAlpine, J.M.K.; Demokan, M.S. Directional sensitivity of a fibre-optic sensor to acoustic signals in transformer oil. In Proceedings of the 4th International Conference on Advances in Power System Control, Operation & Management, Hong Kong, China, 11–14 November 1997; pp. 521–525.
32. Ruan, J.; Deng, Y.; Huang, D.; Duan, C.; Gong, R.; Quan, Y.; Hu, Y.; Rong, Q. HST calculation of a 10 kV oil-immersed transformer with 3D coupled-field method. *IET Electr. Power Appl.* **2020**, *14*, 921–928. [[CrossRef](#)]

33. Amar, M.; Kaczmarek, R. A general formula for prediction of iron losses under nonsinusoidal voltage waveform. *IEEE Trans. Magn.* **1995**, *31*, 2504–2509. [[CrossRef](#)]
34. Linan, R.; Ponce, D.; Betancourt, E.; Tamez, G. Optimized models for overload monitoring of power transformers in real time moisture migration model. *IEEE Trans. Dielectr. Electr. Insul.* **2013**, *20*, 1977–1983. [[CrossRef](#)]
35. Meitei, S.N.; Borah, K.; Chatterjee, S. Review on monitoring of transformer insulation oil using optical fiber sensors. *Results Opt.* **2023**, *10*, 100361. [[CrossRef](#)]

Disclaimer/Publisher’s Note: The statements, opinions and data contained in all publications are solely those of the individual author(s) and contributor(s) and not of MDPI and/or the editor(s). MDPI and/or the editor(s) disclaim responsibility for any injury to people or property resulting from any ideas, methods, instructions or products referred to in the content.